



Dynamics of excitons bound to nitrogen isoelectronic centers in GaAs

P. St-Jean,* G. Éthier-Majcher, and S. Francoeur

Department of Engineering Physics, Polytechnique Montréal, Montréal, Québec, Canada H3C 3A7

(Received 21 December 2014; revised manuscript received 24 February 2015; published 9 March 2015)

A detailed analysis of the dynamics of excitons bound to two nitrogen atoms forming an isoelectronic center of C_{2v} symmetry in GaAs is presented. The temperature dependence of photoluminescence (PL) intensities under both continuous and pulsed excitations reveals (1) overall decay rates significantly slower than that of spontaneous emission, (2) a decay rate anisotropy between states of orthogonal symmetry representations, and (3) a complementary behavior of relative intensities measured from states of identical symmetry representations. A comprehensive model of the exciton fine structure and the exciton dynamics allows the determination of the strength of the exchange and crystal-field interactions, the light- and heavy-hole splitting and composition of exciton states, the exciton capture time, the rates of spontaneous and nonradiative emission, and the rates of interlevel transfers induced by interactions with nuclear spins and by longitudinal acoustic phonons. It is found that the rate of electron spin flips is comparable to that measured in quantum dots but that the near degeneracy of light and heavy holes results in an efficient transfer channel between light- and heavy-hole states of identical symmetry representation.

DOI: [10.1103/PhysRevB.91.115201](https://doi.org/10.1103/PhysRevB.91.115201)

PACS number(s): 78.47.jd, 78.67.-n, 71.35.-y, 71.55.-i

I. INTRODUCTION

The ability to write, manipulate, and read out quantum states is a fundamental requirement for quantum information processing, and over the last decade, several promising optically addressed systems for qubits storage and operations have been identified and studied. Seminal demonstrations were realized using electrostatic and epitaxial quantum dots [1,2], nitrogen-vacancy centers and other defects in diamond [3,4], and phosphorous donors in isotopically purified silicon [5,6]. Each of these systems provides a unique set of advantageous characteristics but also faces a number of challenges, making the evaluation of their long-term prospects for quantum information applications difficult. It is therefore not surprising that the search for other material systems is ongoing. In fact, the choice is wide and remains largely unexplored. This is particularly true for bound states created by impurities or other point defects in crystalline hosts [7–10]. Recently, we have demonstrated that charges trapped on isoelectronic centers (ICs) in semiconductors are promising candidates, as they combine two fundamentally advantageous characteristics not commonly found together: the optical homogeneity of atomic defects and the high dipole moment of semiconductor quantum dots [11].

ICs are atomic defects built from one, two, or a small number of impurities forming an isovalent center. Through a deformation of the lattice and a disruption of the electronic charge density of the host material, this center can trap either an itinerant electron or a hole, depending on the nature of the impurities. This primary charge can then trap via Coulomb interaction a secondary charge of opposite sign to form an exciton. These defects were first studied several decades ago, but the ability to individually address and optically control them has only been demonstrated recently [12]. Although a number of isoelectronic impurities have been identified for many semiconductor materials, pairs of nitrogen atoms (dyads)

in GaAs [12], GaP [13], and AlAs [14] and of Te atoms in ZnSe [15] are the most studied impurity-host systems to date. The physics of ICs is reminiscent of quantum dots since conduction- and valence-band states remain valid for describing bound electrons and holes states. IC characteristics can be tuned by varying the composition (number or type of impurities), configuration (interatomic separation and symmetry), and orientation within the host lattice. They can be addressed both electrically and optically. Furthermore, ICs can bind single charges, excitons, biexcitons, and charged excitons [16], a technological advantage observed for only a very few atomic-size defects [17]. However, in contrast to other optically controlled qubits, their intrinsically low inhomogeneous broadening, high photo-stability, and high electric dipole moments may be strategically advantageous for scaling up quantum information applications with minimal implementation complexity.

To determine their potential as building blocks for quantum information, it is critical to establish a better understanding of IC characteristics (charge-trapping mechanisms, exciton fine structure, energy levels associated with various configurations, etc.) and of the behavior of bound charges. In this work, we reveal several fundamental aspects related to exciton states bound to N dyads in GaAs and their spin dynamics, from the exciton capture rate to interlevel transfer rates. The scope of the experimental data and the depth of the present analysis exceed everything that has previously been done on Te dyads in ZnSe [15] and N dyads in GaAs [18] and GaP [19]. Furthermore, in contrast to many previous works on semiconductor nanostructures [20], this analysis rigorously takes into account the reduced symmetry of the system (C_{2v}) and the considerable light- and heavy-hole mixing of exciton states. It therefore allows for a richer and more complete understanding of the various mechanisms governing the exciton dynamics.

This paper is organized as follows. Section II briefly describes the sample structure and experimental methods used. Section III presents experimental results. It includes the exciton fine structure and the temperature dependence of

*philippe.st-jean@polymtl.ca

time-resolved PL curves and of PL intensities. Section IV presents a comprehensive model used to simulate the exciton dynamics and reproduce the experimental data of Sec. III. Section V demonstrates that this model satisfactorily accounts for all experimental observations and presents an insightful discussion on the important mechanisms governing the exciton dynamics. Finally, Sec. VI briefly summarizes our findings.

II. SAMPLES AND METHODS

A single GaAs:N layer of 25 nm was grown between two 5-nm layers of undoped GaAs(001) and was inserted between two $\text{Al}_{0.25}\text{Ga}_{0.75}\text{As}$ barriers. The concentration of the nitrogen-doped layer is such that the dyad surface density is $1 \mu\text{m}^{-2}$, allowing us to spatially resolve single dyads using a diffraction-limited confocal microscope with a resolution of $0.8 \mu\text{m}$ at 820 nm.

The known nitrogen-dyad configurations that emit in the band gap of GaAs exhibit C_{2v} symmetry [12] and have been assigned to two substitutional nitrogen atoms positioned in first- and fourth-nearest-neighbor sites on the anionic sublattice [21]. In this work, we present emission characteristics of the nitrogen dyad emitting at 1.508 eV, which has been attributed to the first-nearest-anionic-neighbor configuration, NN_1 .

Microphotoluminescence measurements were performed on single dyads at temperatures ranging from 5 to 12 K. Excitation was provided by either a 1-ps mode-locked Ti:sapphire laser operating at 800 nm with a repetition rate of 80 MHz or a cw 780-nm laser. The photoluminescence signal was analyzed using a spectrometer and an avalanche photodiode providing a spectral resolution of $60 \mu\text{eV}$ and a temporal resolution of less than 100 ps. A motorized $\lambda/2$ wave plate and a polarizer were used to analyze the polarization of the emission.

III. EXPERIMENTAL RESULTS

A. Fine structure of the emission

Figures 1(d) and 1(e) show the photoluminescence intensity from a single nitrogen dyad as a function of the energy and linear polarization angle. The fine structure of the excitonic emission arises from the combined effects of confinement, electron-hole exchange interaction, and crystal-field interaction. Although similar to what is usually observed from conventional quantum dots, the quasidegeneracy of heavy- and light-hole states results in a richer fine structure involving twice the number of excitonic states. The specifics of the emission fine structure and polarization can be used to unambiguously identify the symmetry of the dyad [22], as was done for N in GaP [13] and GaAs [12] and for Te dyads in ZnSe [15]. The four transitions presented in Fig. 1 clearly identify a dyad with a C_{2v} symmetry.

Under C_{2v} symmetry, the degeneracy between the eight excitonic states formed by the $J = 2$ quintuplet and the $J = 1$ triplet is completely lifted [16,22]. The mixing of these states gives rise to two dark states ($D_{1,2}$) not coupled to the electromagnetic field and six bright states exhibiting linearly polarized emission: two polarized along the dyad ($X_{1,2}$), two

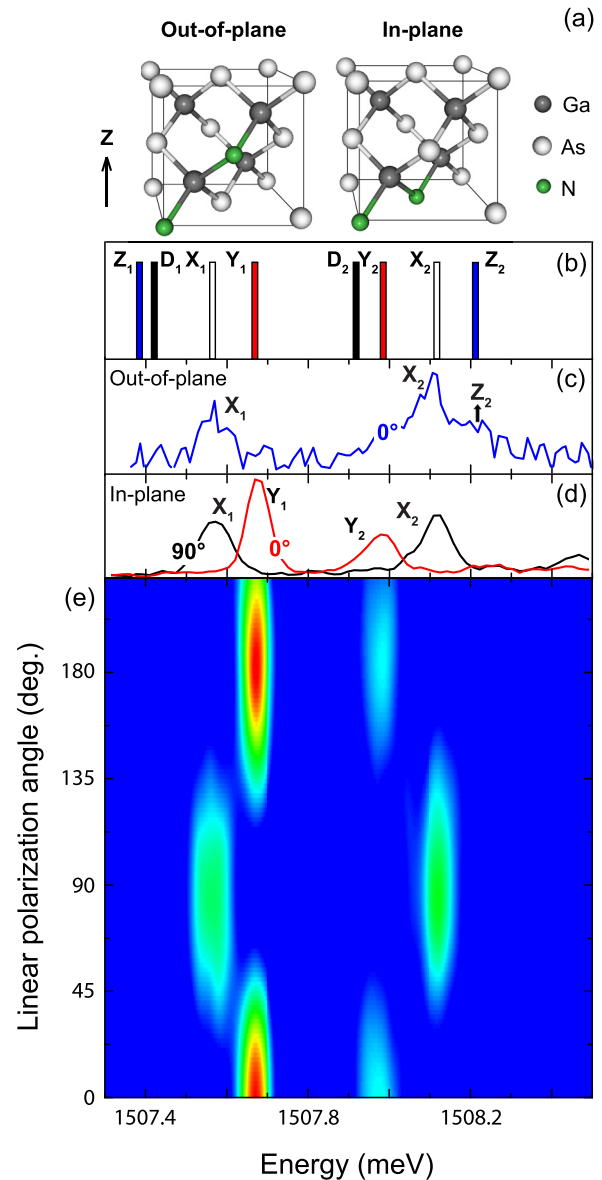


FIG. 1. (Color online) (a) In-plane and out-of-plane configurations for dyads of C_{2v} symmetry. (b) Calculated spectral position of all excitonic states of a nitrogen dyad oriented along $\langle 110 \rangle$. (c) Photoluminescence intensity polarized parallel to an out-of-plane nitrogen dyad of C_{2v} symmetry. (d) Photoluminescence intensity polarized perpendicular (0° , red curve) and parallel (90° , black curve) to the in-plane nitrogen dyad studied in this work. (e) Photoluminescence intensity map as a function of linear energy and linear polarization of the emission.

polarized perpendicular to the dyad and the C_2 axis ($Y_{1,2}$), and two polarized along the C_2 axis ($Z_{1,2}$).

Transitions in the spectra of Fig. 1 are labeled according to the orientation of their polarization (X, Y, Z) and to their relative energy (1 and 2 for the low- and high-energy manifolds, respectively). The absence of $Z_{1,2}$ transitions in the spectra shown in Figs. 1(d) and 1(e) indicates that this particular center is formed from two nitrogen atoms located in the plane of the sample and oriented along $\langle 110 \rangle$. Transition Z_2 is observed only from out-of-plane dyads, for which a PL

spectrum is presented in Fig. 1(c) in order to complete the set of optical transitions observed from this isoelectronic center configuration [23].

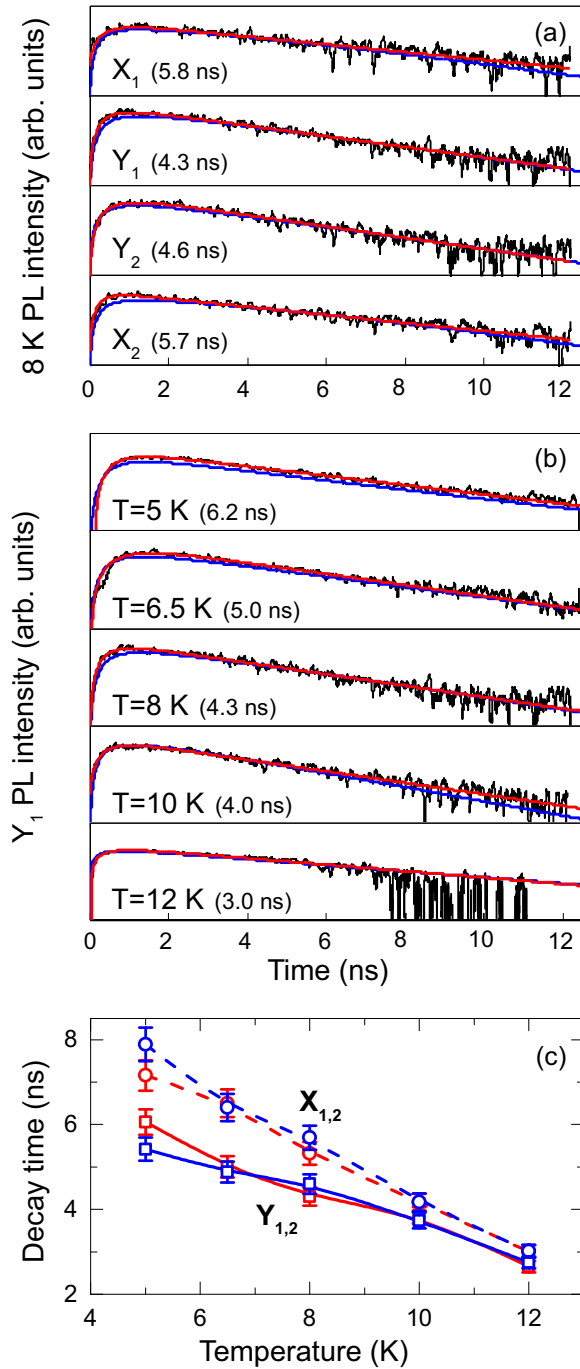


FIG. 2. (Color online) Time-resolved PL from the single nitrogen dyad presented in Fig. 1. (a) All four excitonic transitions at $T = 8$ K and (b) transition Y_1 at all temperatures studied. For both panels, the red curves show the sum of one rising and one decaying monoexponential that best fitted the data; decay times are indicated. Blue curves show the PL intensities calculated from the model presented in Sec. IV. (c) Temperature evolution of extracted decay times. Y_1 and Y_2 (X_1 and X_2) are represented by the red and blue squares (circles). Dashed (X_i) and solid (Y_i) lines are added to guide the eye.

B. Luminescence decay-time anisotropies

Time-resolved photoluminescence (TRPL) was performed on X_1 , X_2 , Y_1 , and Y_2 at temperatures of 5, 6.5, 8, 10, and 12 K. Above 12 K, the photoluminescence intensity abruptly vanishes. Figure 2 presents a representative subset of the data used in this work to analyze the exciton dynamics: Fig. 2(a) shows the TRPL curves of the four allowed transitions at 8 K, and Fig. 2(b) shows the TRPL curves of Y_1 at all temperatures studied. As can be seen from the two panels, all curves are very well represented by the sum of one rising and one decaying monoexponential (red curves). This was also the case for the 12 other PL decay curves.

The rise time of the photoluminescence varies between 250 and 500 ps and does not exhibit a dependence on temperature or on the excitonic state involved, indicating that the exciton or charge-carrier capture process does not sensitively depend on these two aspects for the temperature range studied. In contrast, the decay time of the luminescence significantly depends on both. As indicated in Fig. 2(a), at 8 K, the decay times of X_1 and X_2 are, respectively, 5.8 and 5.7 ns, and those of Y_1 and Y_2 are, respectively, 4.3 and 4.6 ns. Interestingly, decay times of states involving identical polarizations are quite similar, but they strongly differ for states involving orthogonal polarizations. This decay-time *anisotropy* is very well illustrated in Fig. 2(c), as it is observed at all temperatures, although most significantly at low temperatures.

In addition to this anisotropy, we note that the measured PL decay times are about 10 times slower than the anticipated spontaneous emission lifetimes. Determined from resonantly driven Rabi oscillations, dipole moments reveal radiative lifetimes on the order of 500 ps [11].

C. Revealing symmetries in photoluminescence intensities

Relative luminescence intensities as a function of temperature exhibit surprisingly rich information also pertaining to the exciton dynamics. Figure 3(a) presents the relative intensity of the four transitions, and Fig. 3(b) shows the

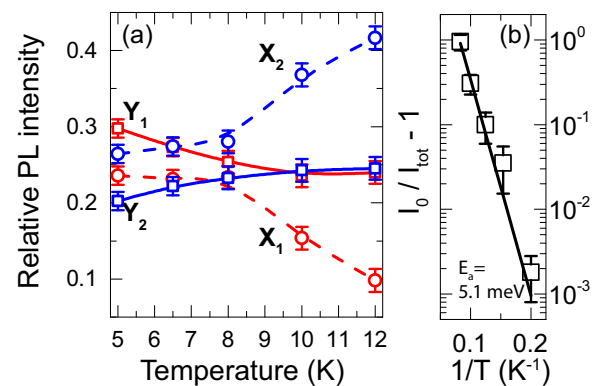


FIG. 3. (Color online) (a) Temperature dependence of the relative PL intensity of the four allowed excitonic transitions. Y_1 and Y_2 (X_1 and X_2) are represented by the red and blue squares (circles). Dashed (X_i) and solid (Y_i) lines are added to guide the eye. (b) Arrhenius plot of the total PL intensity measured from all four transitions shown in Fig. 1. The solid curve shows the calculated intensity of a thermally activated process.

evolution of the total intensity. Relative intensities show distinctive behaviors depending on both the transition energy and polarization. Intensities of $X_{1,2}$ are almost equal at 5 K, but the higher-energy X_2 strongly dominates the lower-energy X_1 at higher temperatures. In contrast, transitions $Y_{1,2}$ show dissimilar intensities at 5 K, but their intensities converge at higher temperatures. At all temperatures, the sum of the intensity of X_1 and X_2 and that of Y_1 and Y_2 make up 50% of the total intensity.

D. Quenching of the photoluminescence total intensity

Figure 3(b) shows an Arrhenius plot of the total intensity measured from the four allowed transitions as a function of temperature. A rapid intensity drop of more than 3 orders of magnitude is observed as temperature is raised from 5 to 12 K. It is due to thermally activated nonradiative processes quenching the radiative emission. Finally, all experimental results presented in this section are representative of those measured on other nitrogen dyads emitting at 1.508 eV.

IV. EXCITON DYNAMICS MODEL

Identical decay times for similarly polarized transitions together with striking symmetries in photoluminescence intensities suggests that efficient $X_1 \leftrightarrow X_2$ and $Y_1 \leftrightarrow Y_2$ transfers occur before radiative emission. Furthermore, the X and Y decay-time anisotropy along with the fact that all decay times measured significantly exceed spontaneous emission lifetimes suggests that recombination dynamics is also influenced by a second interlevel transfer mechanism connecting bright and dark states together. Although valuable clues can be directly extracted from the data, a comprehensive understanding of the exciton dynamics requires a quantitative model. In this section, we present the model used to analyze the time and temperature dependence of the PL, extract information on the angular component of exciton wave functions, reproduce exciton transition energies, and determine radiative and nonradiative rates along with interlevel transfer rates.

Figure 4 presents the structure of the model and the parameters (shown inside gray boxes) required to numerically reproduce the experimental data (labeled in red). This model is divided in three parts. Part I calculates exciton energies and wave functions from a Hamiltonian that takes into account the exchange and the crystal-field interactions and light- and heavy-hole confinement effects. A rigorous treatment of C_{2v} symmetry requires six parameters. Part II uses these wave functions to calculate transfer rates associated with spontaneous emission and nonradiative emission and interlevel transfer rates induced by the hyperfine interaction and by acoustic phonons. The relative influence of these four mechanisms is modulated by five parameters: $\Gamma_0^{(\text{rad})}$, $\Gamma_0^{(\text{nr})}$, $W_0^{(\text{hf})}$, $\Gamma_0^{(\text{ap})}$, and the energy barrier E_f associated with the nonradiative process. Except for spontaneous emission, exciton transfers are thermally activated and sensitively depend on temperature. Finally, part III dynamically calculates exciton populations and PL intensities using a nine-level population balance model. It exploits the transfer rates calculated in part II with the addition of a parameter describing the exciton capture rate $\Gamma^{(\text{capt})}$. Here, we present a detailed description of these three parts.

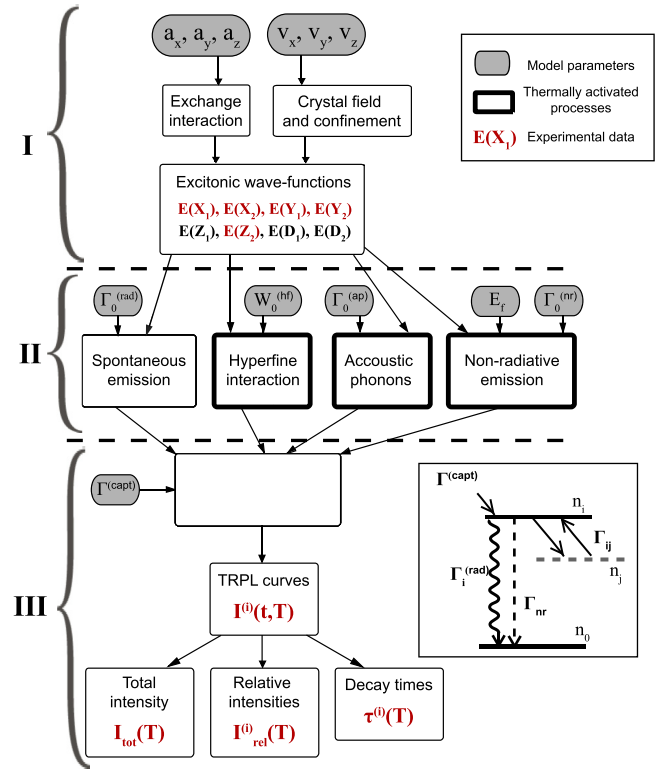


FIG. 4. (Color online) Schematic representation of the model used to calculate excitonic energies and wave functions, time-resolved luminescence curves, and luminescence intensities. Quantities in gray boxes are adjustable parameters, and quantities labeled in red are those directly compared to the experimental data. Boxes with thicker contours indicate temperature-dependent transfer mechanisms. The inset shows the population balance model for excitonic state i involving the ground state 0 and the seven other excitonic states for which $i \neq j$.

A. Part I: Excitonic wave functions

The perturbation Hamiltonian lifting the degeneracy between the eight states of the bound exciton takes into account three effects: the electron-hole exchange interaction, the crystal-field perturbation produced by the dyad on the crystal, and the confinement effects experienced by light and heavy holes.

Under C_{2v} symmetry, the three principal axes are inequivalent, and the Hamiltonian is

$$H = - \sum_{i=x,y,z} a_i J_i S_i + \sum_{i=x,y,z} v_i J_i^2, \quad (1)$$

where \mathbf{J} and \mathbf{S} represent the total angular momentum of the hole and the electron spin. The first term in the Hamiltonian corresponds to the exchange interaction, where $a_{x,y,z}$ are the nondegenerate exchange parameters. Similarly, the crystal-field Hamiltonian is composed of three coefficients, $v_{x,y,z}$. The diagonal part of this Hamiltonian is isomorphic to the effect of confinement on light- and heavy-hole bands, such that these coefficients also take into account effects of confinement on the exciton fine structure. More details about the development of this Hamiltonian can be found in Ref. [22].

TABLE I. Symmetry-adapted exciton wave functions, C_{2v} representations, and dipole moments [expressed in units of $(\langle s|x|x\rangle, \langle s|y|y\rangle, \langle s|z|z\rangle)$]. ψ_{1-4} and ψ_{5-8} are built from heavy- and light-hole states, respectively.

| Wave function | Representation | $\langle \psi_i \hat{\mathbf{r}} 0 \rangle$ |
|--|----------------|---|
| $\psi_1^{(z)} = \frac{1}{\sqrt{2}}(-\beta_e \phi_4 + \alpha_e \phi_1)$ | Γ_1 | (0,0,0) |
| $\psi_2^{(x)} = \frac{1}{\sqrt{2}}(\beta_e \phi_1 + \alpha_e \phi_4)$ | Γ_2 | $(\frac{1}{\sqrt{2}}, 0, 0)$ |
| $\psi_3^{(d)} = \frac{i}{\sqrt{2}}(\beta_e \phi_4 + \alpha_e \phi_1)$ | Γ_3 | (0,0,0) |
| $\psi_4^{(y)} = \frac{i}{\sqrt{2}}(-\beta_e \phi_1 + \alpha_e \phi_4)$ | Γ_4 | $(0, \frac{1}{\sqrt{2}}, 0)$ |
| $\psi_5^{(z)} = \frac{1}{\sqrt{2}}(-\beta_e \phi_2 + \alpha_e \phi_3)$ | Γ_1 | $(0, 0, \frac{2}{\sqrt{3}})$ |
| $\psi_6^{(x)} = \frac{1}{\sqrt{2}}(\beta_e \phi_3 + \alpha_e \phi_2)$ | Γ_2 | $(\frac{-1}{\sqrt{6}}, 0, 0)$ |
| $\psi_7^{(d)} = \frac{i}{\sqrt{2}}(\beta_e \phi_2 + \alpha_e \phi_3)$ | Γ_3 | (0,0,0) |
| $\psi_8^{(y)} = \frac{i}{\sqrt{2}}(-\beta_e \phi_3 + \alpha_e \phi_2)$ | Γ_4 | $(0, \frac{1}{\sqrt{6}}, 0)$ |

The remote spin-orbit split-off valence states are ignored, and this Hamiltonian is expanded in a basis of eight excitonic states built from two electron states ($\alpha_e = |1/2, 1/2\rangle$, $\beta_e = |1/2, -1/2\rangle$) and four hole states ($\phi_1 = |3/2, 3/2\rangle$, $\phi_2 = |3/2, 1/2\rangle$, $\phi_3 = |3/2, -1/2\rangle$, and $\phi_4 = |3/2, -3/2\rangle$). Symmetry-adapted exciton wave functions are presented in Table I and Fig. 5 along with their representations and dipole moments. ψ_{1-4} and ψ_{5-8} are, respectively, built from light- and heavy-hole states, and superscripts (x , y , z , or d) indicate either the polarization orientation or a dark state not interacting with the radiation through the usual dipolar term.

Exciton energies and wave functions are obtained by diagonalizing Eq. (1). Mixing between light- and heavy-hole states of identical representations generates eight coupled wave functions Ψ_i . This approach has already been used to analyze the excitonic fine structure of in-plane [24] and out-of-plane nitrogen dyads [23].

B. Part II: Exciton transfer mechanisms

Exciton energies and wave functions are then used to calculate transfer rates associated with spontaneous emission to the ground states, nonradiative processes, and interlevel transfers.

1. Spontaneous emission and nonradiative processes

The rate of spontaneous emission from the excitonic state $|\Psi_i\rangle$ to the ground state $|0\rangle$ is calculated

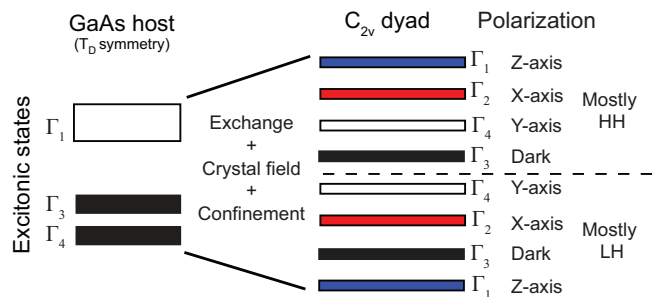


FIG. 5. (Color online) Schematic diagrams of energy levels for a free exciton in a GaAs crystal and for an exciton bound to a nitrogen dyad of C_{2v} symmetry. The ordering of the levels is obtained from Eq. (1) and the PL data.

using

$$\Gamma_i^{(\text{rad})} = \Gamma_0^{(\text{rad})} |\langle \Psi_i | \hat{\mathbf{r}} | 0 \rangle|^2. \quad (2)$$

where $\hat{\mathbf{r}}$ is a vector of unit length. In this expression, the radial parts of atomic and envelope wave functions were decoupled from angular and spin coordinates and were absorbed into $\Gamma_0^{(\text{rad})}$, which is to be determined experimentally. The angular part $\langle \Psi_i | \hat{\mathbf{r}} | 0 \rangle$ is explicitly integrated to obtain the relative dipole moment of excitonic transition i .

As shown in Fig. 3(b), the total PL intensity is strongly influenced by temperature, indicating the presence of thermally activated nonradiative processes. Assuming the presence of an external state f positioned at energy E_f , the nonradiative rate for state i is

$$\Gamma_i^{(\text{nr})} = \frac{\Gamma_0^{(\text{nr})}}{\exp(\Delta E_i / k_B T) - 1}, \quad (3)$$

where $\Delta E_i = E_f - E_i$ is the activation energy associated with the transfer from i to state f . $\Gamma_0^{(\text{nr})}$ is a constant describing the strength of phonon-exciton interactions enabling nonradiative processes. It does not depend on the exciton state, and it is determined experimentally.

2. Interlevel transfers mechanism

Interlevel transfers between excitonic states involve processes flipping the spin of the electron or hole or both. The most relevant spin-flip mechanisms for isoelectronic centers are discussed below.

Spin-orbit-induced transfers. The spin relaxation of electrons (~ 100 ps) and holes (~ 100 fs) in bulk semiconductors is dominated by spin-orbit interaction [25,26]. In quantum dots, much longer relaxation times are experimentally found at low temperatures, revealing that carrier localization strongly quenches spin-orbit-related mechanisms [27–32]. Indeed, theoretical calculations estimate that spin-orbit interaction leads to electron and hole spin-relaxation times exceeding $1 \mu\text{s}$ in strongly confined quantum dots (≤ 10 nm) [33–35]. Although the localization of electrons bound to ICs like N dyads in GaAs is not accurately known, two important aspects indicate a strong localization: the rapid variation of the exciton binding energy with the separation between the two nitrogen atoms [36] and the very small diamagnetic [37] shift ($1.27 \mu\text{eV T}^{-2}$) associated with the bound electron [24]. Furthermore, empirical pseudopotential calculations suggest that the electron wave function is concentrated within the volume of a few unit cells [21]. Spin-orbit-related processes are thus expected to be of secondary importance.

Hyperfine-induced transfers. The dominant electron spin-relaxation mechanism in semiconductor quantum dots is the simultaneous spin flip of an electron and a nucleus induced by the hyperfine interaction [38,39]. The calculation of transfer rates between nondegenerated excitonic states requires second-order perturbation theory because the energy involved in the spin flip of a nuclear spin does not match the exciton energy splitting [40,41] and a phonon interaction is necessary to fulfill energy conservation. Analytical models reveal that the rates are inversely proportional to N , the number of nuclei under the electron wave function. Therefore, in comparison with quantum dots where $N \sim 10^5$, the strong localization

of the electron mentioned above could lead to very efficient hyperfine-induced exciton transfers.

The calculation of transfer rates starts from the Hamiltonian describing the hyperfine contact interaction between a bound electron and nearby lattice nuclei,

$$\begin{aligned} H^{(\text{hf})} &= \sum_k A_k \mathbf{S} \cdot \mathbf{I}_k \\ &= \sum_k A_k \left(\frac{1}{2} (S_+ I_{-,k} + S_- I_{+,k}) + S_z I_{z,k} \right), \end{aligned} \quad (4)$$

where the summation runs over all nuclei sites. $A_k = A_{0,k} v_0 |\Psi(\mathbf{r}_k)|^2$, where $A_{0,k}$ are the hyperfine constants, v_0 is the primitive cell volume, and $|\Psi(\mathbf{r}_k)|^2$ is the electron density at site k . \mathbf{S} and \mathbf{I}_k are the electron and nucleus spin operators, and S_{\pm} and I_{\pm} are the usual ladder operators. Since they have been shown to be less efficient, spin flips involving holes and nuclei are neglected [42,43].

The first two terms in Eq. (4) lead to electron-nucleus spin flips. The nuclear spin-flip energy $\hbar\omega_n$ is negligible compared to the energy difference between exciton states, and interlevel transfers must be assisted by phonon emission or absorption $\hbar\omega_q$. The transfer rate is therefore determined by both the hyperfine ($H^{(\text{hf})}$) and exciton-phonon ($H^{(\text{ph})}$) interactions. Using second-order perturbation and Fermi's golden rule, the transfer rate from $|\Psi_i\rangle$ to $|\Psi_j\rangle$ is

$$\Gamma_{ij}^{(\text{hf})} = \Gamma_0^{(\text{ph})} \sum_{\mu, \mu'} P(\mu) \left| \frac{\langle \Psi_v, \mu' | H^{(\text{hf})} | \Psi_i, \mu \rangle}{E_{ij}} \right|^2, \quad (5)$$

where

$$\begin{aligned} \Gamma_0^{(\text{ph})} &= \frac{2\pi}{\hbar} |\langle \Psi_j | H^{(\text{ph})} | \Psi_v \rangle|^2 \delta(E_i - E_j) \\ &\times \begin{cases} N_B(E_{ij}) & \text{if } E_j > E_i, \\ N_B(E_{ij}) + 1 & \text{otherwise} \end{cases} \end{aligned} \quad (6)$$

is the phonon-exciton scattering rate, $N_B(E_{ij})$ is the phonon occupation probability given by the Bose-Einstein statistic, $|\Psi_v\rangle$ is a virtual state with angular component similar to that of Ψ_j , and $E_{ij} = |E_j - E_i|$. $E_j > E_i$ corresponds to phonon absorption, and $E_j < E_i$ corresponds to phonon emission. μ and μ' refer to the initial and final nuclear-spin states, and $P(\mu)$ is their occurrence probability. In the absence of nuclear polarization, $P(\mu)$ is the same for all possible values of μ . Equation (5) is simplified by collecting into a single parameter, $W_0^{(\text{hf})}$, all quantities independent of the excitonic states involved. This includes normalization constants arising from the radial and envelope parts of wave functions, hyperfine constants A_k , and physical constants. In addition, the phonon-exciton interaction is assumed to be identical for all states j , such that the influence of $\langle \Psi_j | H^{(\text{ph})} | \Psi_v \rangle$ is also collected in $W_0^{(\text{hf})}$. The hyperfine transfer rate is thus given by

$$\begin{aligned} \Gamma_{ij}^{(\text{hf})} &= W_0^{(\text{hf})} \sum_{\mu, \mu'} P(\mu) \left| \frac{\langle \Psi_j, \mu' | (S_+ I_- + S_- I_+) | \Psi_i, \mu \rangle}{E_{ij}} \right|^2 \\ &\times \begin{cases} N_b(E_{ij}) & \text{if } E_j > E_i, \\ N_b(E_{ij}) + 1 & \text{otherwise.} \end{cases} \end{aligned} \quad (7)$$

Matrix elements are evaluated using wave functions $|\Psi_i\rangle$, and as expected, nonvanishing transfer rates occur between dark or Z -polarized states and X - or Y -polarized states. The value for $W_0^{(\text{hf})}$ is determined by fitting the model to the experimental data.

Acoustic-phonon-induced transfers. For epitaxial quantum dots, valence-band degeneracy is lifted by confinement and external strains, leading to negligible exciton transfers between light- and heavy-hole manifolds [44]. For isoelectronic centers, the Hamiltonian presented in Eq. (1) couples nearly degenerate light- and heavy-hole excitonic states, and as a result, new processes can significantly influence the exciton dynamics.

Through their deformation of the lattice, phonons create a momentary perturbation providing the impulse and energy needed for interlevel exciton transfers. These exciton-phonon interactions arise principally through the piezoelectric and deformation potential couplings generated by acoustic phonons, but for exciton states, piezoelectric coupling is relatively unimportant because the electron and hole wave-function overlap reduces polar interactions [45,46]. Deformation potential coupling is treated using the Bir-Pikus strain Hamiltonian, which, for a system of C_{2v} symmetry, is

$$\begin{aligned} H^{(\text{dp})} &= 4 \sum_{i=x,y,z} (d_{xi} J_x^2 + d_{yi} J_y^2 + d_{zi} J_z^2) \langle \epsilon_{ii} \rangle \\ &+ \frac{2}{\sqrt{3}} (e_{xz} \{J_x, J_z\} \langle \epsilon_{xz} \rangle + e_{yz} \{J_y, J_z\} \langle \epsilon_{yz} \rangle \\ &+ e_{xy} \{J_x, J_y\} \langle \epsilon_{xy} \rangle), \end{aligned} \quad (8)$$

where the notation $\{J_i, J_j\}$ denotes an anticommutator, d_{ij} and e_{if} are deformation potentials, and $\langle \epsilon_{ij} \rangle$ are phonon-induced strains averaged over the hole wave function. This Hamiltonian couples any given heavy-hole (light-hole) state with its light-hole (heavy-hole) counterpart of identical representation through longitudinal strain elements ϵ_{ii} and with the three remaining light-hole (heavy-hole) states through shear strain elements ϵ_{ij} ($i \neq j$). Simplifications are necessary to reduce the complexity of this Hamiltonian to a tractable level. First, it has been demonstrated that deformation potential coupling is dominated by LA phonons [47,48], as long wavelength TA phonons are akin to lattice translations at the scale of a localized exciton. Thus, coupling induced by TA phonons through shear components are neglected by setting $d_{ij} = 0$ for $i \neq j$. This assumption implies that transfers can now occur between only light- and heavy-hole states of similar symmetry representations. The next simplification consists of assuming that deformation potentials are simply proportional to the crystal-field parameters solutions of Eq. (1), $d_{ii} = d v_i$. These simplifications lead to

$$H^{(\text{df})} = 4d (v_x J_x^2 + v_y J_y^2 + v_z J_z^2) (\langle \epsilon_{xx} \rangle + \langle \epsilon_{yy} \rangle + \langle \epsilon_{zz} \rangle). \quad (9)$$

By combining d , strain components, and all other constants into a single parameter $\Gamma^{(\text{ap})}$, the transfer rate from $|\Psi_i\rangle$ to $|\Psi_j\rangle$

induced by LA phonons is then

$$\Gamma_{ij}^{(\text{ap})} = \Gamma_0^{(\text{ap})} |\langle \Psi_i | H^{(dp)} | \Psi_j \rangle|^2 \times \begin{cases} N_B(E_{ij}) & \text{if } E_j > E_i, \\ N_B(E_{ij}) + 1 & \text{otherwise.} \end{cases} \quad (10)$$

As will be seen, this light- and heavy-hole coupling explains the efficient population transfer between bright states of identical polarizations.

C. Part III: Population balance model

The time evolution of the population of all eight excitonic states can be obtained by solving nine coupled differential equations. The population balance model schematically represented in the inset of Fig. 4 leads to eight equations of the form

$$\frac{dn_i}{dt} = - \left[\Gamma_i^{(\text{rad})} + \Gamma_i^{(\text{nr})} + \sum_{j \neq i} (\Gamma_{ij}^{(\text{hf})} + \Gamma_{ij}^{(\text{ap})}) \right] n_i + \sum_{j \neq i} (\Gamma_{ji}^{(\text{hf})} + \Gamma_{ji}^{(\text{ap})}) n_j + \Gamma^{(\text{capt})} n_0 \quad (11)$$

and

$$\frac{dn_0}{dt} = - \left(\sum_i \Gamma^{(\text{capt})} \right) n_0, \quad (12)$$

where n_i is the population of state i ($i = 1-8$) and n_0 is the exciton reservoir population. Index j runs over the indices of all other states for which $j \neq i$. $\Gamma^{(\text{capt})}$ is the exciton capture rate, which is, in this model, identical for all states and independent of temperature. All other transfer rates were defined earlier.

These equations are solved numerically as a function of time and temperature using $n_0 = 1$ and $n_i = 0$ for initial conditions. The time evolution of exciton populations are calculated with time increments of 4 ps. The instantaneous PL intensities given by

$$I_i(t, T) = n_i(t, T) \Gamma_i^{(\text{rad})} \quad (13)$$

can be directly compared with experimental TRPL curves and decay times $\tau(T)$. The PL intensity under continuous excitation is obtained by time integrating $I(t, T)$.

V. RESULTS AND ANALYSIS

The model parameters listed in Fig. 4 were determined in two phases. First, the exchange and crystal-field coefficients were deduced from the observed optical transition energies and three additional physical considerations. Then, the parameters describing the exciton dynamics were determined by *simultaneously* fitting all experimental time decay curves and intensities.

A. Excitonic fine structure

A reliable determination of exchange (a_i) and crystal-field (v_i) coefficients minimally requires six conditions. The first set of conditions is provided by the five transition energies shown in Fig. 1: $X_{1,2}$ and $Y_{1,2}$ measured from an in-plane dyad and

Z_2 measured from an out-of-plane dyad. Z_1 is associated with a very low oscillator strength in high-quality samples, and its energy position could not be reliably determined.

A second set of conditions is obtained from these three additional considerations. First, the average value of exchange coefficients must be positive, such that dark (triplet) states are pushed below bright (singlet) states. Second, the dyad orientation with respect to the measurement axes is obtained from the polarization information gathered from both in-plane and out-of-plane dyads. This identification allows associating with each transition the required wave-function symmetry representation and restricts the range of values for the exchange and crystal-field coefficients [23]. Finally, we use the fact that the relative intensities of Y_1 and Y_2 plateau at 25% for $T > 10$ K (see Fig. 3). In this temperature regime, the thermal energy ($> 1000 \mu\text{eV}$ at 12 K) overcomes the energy difference between Y_1 and Y_2 ($180 \mu\text{eV}$) such that the exciton occupation probability is uniformly distributed over both states. Populations can then be factored out of Eq. (13), and relative intensities are determined by spontaneous emission rates or, according to Eq. (2), by their dipole moments. Equal intensities therefore imply

$$|\langle Y_1 | \hat{\mathbf{r}} | 0 \rangle|^2 = |\langle Y_2 | \hat{\mathbf{r}} | 0 \rangle|^2. \quad (14)$$

This condition sets the relative weight of light- and heavy-hole components of Y_1 and Y_2 , and because the sums of light- and heavy-hole components are conserved, it affects the energy and wave function of the other six states. It considerably narrows down the range of admissible values and facilitates the search of the optimal solution.

These two sets of conditions are used to extract the following values of the exchange and crystal-field coefficients:

$$\begin{aligned} a_x &= 142.0 \mu\text{eV}, & a_y &= 202.0 \mu\text{eV}, & a_z &= 180.8 \mu\text{eV}, \\ v_x &= 116.0 \mu\text{eV}, & v_y &= 198.4 \mu\text{eV}, & v_z &= -82.4 \mu\text{eV}. \end{aligned}$$

As can be seen from Figs. 1(b) and 1(d), precise agreement between calculated (vertical rectangles) and experimental energy values is obtained.

In Ref. [24], the uncertainty in the value of exchange and crystal-field coefficients was estimated to be less than 25%. We believe that the values reported here are more accurate since additional restrictions were taken into account, such as the intensity ratio Y_1/Y_2 and the spectral position of Z_2 . A small variation of the coefficients did not significantly affect energies and wave functions, and the uncertainty is estimated at about 10%.

Although D_{2d} or other higher-symmetry versions of Eq. (1) could not satisfactorily reproduce experimental results, the three exchange coefficients are, nonetheless, relatively similar and differ by less than 20% from their average value ($182 \mu\text{eV}$). In addition to strain produced by the dyad in its environment, crystal-field coefficients indirectly take into account light- and heavy-hole confinement effects. The light- and heavy-hole splitting resulting from strain and confinement is $v_x + v_y - 2v_z$, leading to a value of $474 \mu\text{eV}$. This energy splitting is considerably larger than the exchange energy, indicating that the exciton states preserve a dominant light- or heavy-hole character. In contrast, the exchange interaction

TABLE II. Calculated wave functions, energies, and relative dipole moments of excitons bound to a dyad of C_{2v} symmetry. The PL energies are relative to the state with the lowest emission energy, $|Z_1\rangle$. States ψ_{1-8} are presented in Table I.

| Wave function Ψ_i | PL energy (μeV) | Relative dipole moment |
|--|------------------------------|------------------------|
| $ Z_2\rangle = 0.115\psi_1 + 0.993\psi_5$ | 854.7 | 0.33 |
| $ X_2\rangle = 0.449\psi_2 + 0.894\psi_6$ | 721.7 | 0.24 |
| $ Y_2\rangle = -0.259\psi_4 + 0.957\psi_8$ | 571.7 | 0.17 |
| $ D_2\rangle = -0.092\psi_3 - 0.996\psi_7$ | 503.5 | 0 |
| $ Y_1\rangle = -0.966\psi_4 - 0.259\psi_8$ | 261.7 | 0.17 |
| $ X_1\rangle = 0.894\psi_2 - 0.449\psi_6$ | 171.7 | 0.10 |
| $ D_1\rangle = -0.996\psi_3 + 0.092\psi_7$ | 7.1 | 0 |
| $ Z_1\rangle = -0.993\psi_1 + 0.115\psi_5$ | 0 | 4×10^{-3} |

dominates the crystal field and confinement effects for nitrogen dyads in GaP [19].

The solution to Eq. (1) also provides excitonic wave functions. They are given in Table II, along with their energy and relative dipole moment. Excitonic states can be divided into two groups: the low-energy (high-energy) group Ψ_1 (Ψ_2) shows a dominant heavy-hole (light-hole) character, illustrating again that crystal-field and confinement effects dominate the exchange interaction. The heavy- and light-hole mixing is relatively important for X and Y states, as was observed in quantum dots [49], but it is particularly weak for D and Z states. We will therefore refer to states X_1 , Y_1 , Z_1 , and D_1 as *heavy-hole* states and to states X_2 , Y_2 , Z_2 , and D_2 as *light-hole* states.

As expected, the relative oscillator strength is distributed equally along the three polarization directions. Interestingly, light-hole excitons Ψ_2 gather 3 times the oscillator strength of heavy-hole excitons Ψ_1 .

B. Exciton dynamics

The six parameters related to the exciton dynamics were determined by *simultaneously* fitting the experimental data set composed of 20 TRPL curves and 20 integrated intensities. They are listed in Table III. Their determination was facilitated by the distinctive effects each transfer mechanism has on decay times and relative intensities and by their relative importance as a function of temperature.

As shown by the blue decay curves in Fig. 2, the calculated time evolutions reproduce those of the four allowed transitions at 8 K and that of Y_1 at all five temperatures. As already mentioned, only a fraction of the data experimentally measured and numerically modeled is shown, but the agreement is just as satisfactory for the 12 other TRPL curves. The experimental decay times shown in Fig. 2(c) are reproduced and compared to calculated values in Fig. 6(a). As can be seen, the calculated

TABLE III. Parameters describing the exciton dynamics.

| $\Gamma_0^{(\text{capt})}$ (ns^{-1}) | $\Gamma_0^{(\text{rad})}$ (ns^{-1}) | $\Gamma_0^{(\text{nr})}$ (ns^{-1}) | E_f (meV) | $\Gamma_0^{(\text{ap})}$ (ns^{-1}) | $W_0^{(\text{hf})}$ ($\mu\text{eV}^2 \text{ns}^{-1}$) |
|--|---|--|----------------|--|--|
| 0.051 | 15.4 | 151 | 4.7 | 4.2 | 263 |

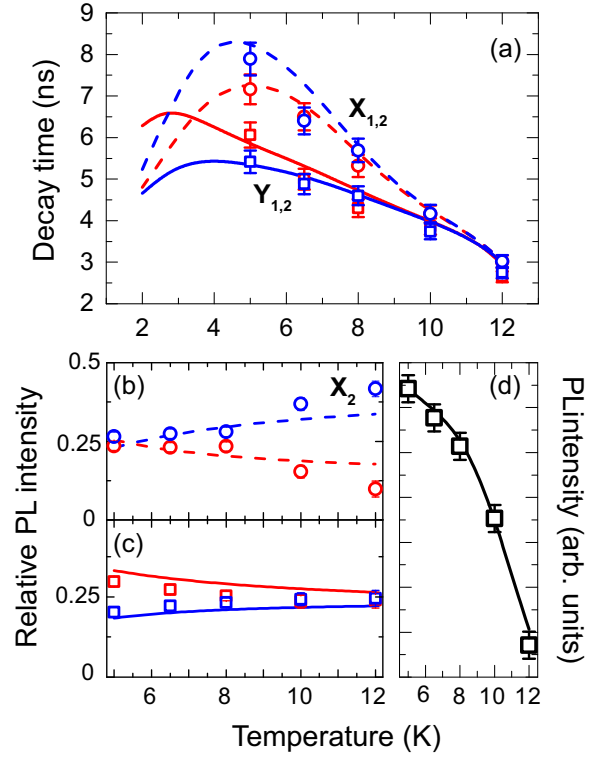


FIG. 6. (Color online) (a) Comparison of the temperature dependence of experimental and calculated TRPL decay times. The relative photoluminescence intensities of (b) $X_{1,2}$ and (c) $Y_{1,2}$ (error bars are too small to be visible). (d) The total photoluminescence intensity. Data points and curves represent experimental and calculated values, respectively.

decay times reproduce all important aspects of the experimental data set: (1) the distinctive decay time associated with all transitions at $T \leq 5$ K, (2) the convergence of the decay time associated with similarly polarized transitions at higher temperatures, (3) the decay-time anisotropy between X and Y transitions at $T \leq 10$ K, and (4) the vanishing anisotropy at higher temperatures. The model also satisfactorily reproduces the relative intensity of all four transitions as a function of temperature. As can be seen in Figs. 6(b) and 6(c), Y_1 (X_2) dominates the spectra at low (high) temperatures, X (Y) transitions show equal intensities at low (high) temperatures, and X and Y transitions make half of the total intensity. Finally, the calculated PL intensity shown in Fig. 6(d) accurately reproduces the effect of the temperature-dependent quenching mechanism. As the model satisfactorily captures all aspects of the experimental data, an in-depth interpretation of the exciton dynamics is possible.

1. Exciton capture

The capture rate $\Gamma_0^{(\text{capt})}$ represents the rate at which a given state is populated by an exciton. The rate at which a dyad binds an exciton in any of the eight excitonic states is 8 times superior, leading to a capture time of 2.5 ns. This capture time is long compared to that of quantum dots, which typically occurs on a time scale of 100 ps. Although the exciton formation mechanism is not yet well understood, the

TABLE IV. Exciton transfer rates (in ns⁻¹). All temperature-dependent rates are given at 5 (upper entry) and 12 K (lower entry). Transfers resulting from the coupling of light and heavy holes through LA phonons are shown in *italic*. All other interlevel rates results from the hyperfine interaction.

| From | To | | | | | | | | Radiative rate | Nonradiative rate |
|---------------|--|--|--|-------------------------------|--|--|--|--|----------------|-----------------------------|
| | $ Z_2\rangle$ | $ X_2\rangle$ | $ Y_2\rangle$ | $ D_2\rangle$ | $ Y_1\rangle$ | $ X_1\rangle$ | $ D_1\rangle$ | $ Z_1\rangle$ | | |
| $ Z_2\rangle$ | | 0.20 0.45 | 0.0063 0.012 | 0 | 4.7×10^{-4} 8.2×10^{-4} | 2.3×10^{-4} 3.6×10^{-4} | 0 | <i>0.097</i> <i>0.15</i> | 5.1 | 0.0028 1.6 |
| $ X_2\rangle$ | 0.16 0.41 | | 0 | 0.0091 0.018 | 0 | <i>14.0</i> <i>24.4</i> | 1.3×10^{-4} 2.1×10^{-4} | 2.1×10^{-4} 3.2×10^{-4} | 3.7 | 0.0020 1.4 |
| $ Y_2\rangle$ | 0.0028 0.0087 | 0 | | 0.66 1.5 | 29.5 <i>58.4</i> | 0 | 6.4×10^{-4} 0.0011 | 4.7×10^{-4} 8.2×10^{-4} | 2.6 | 0.0014 1.2 |
| $ D_2\rangle$ | 0 | 0.0044 0.013 | 0.57 1.4 | | 0.035 0.077 | 0.0011 0.0021 | <i>0.43</i> <i>0.77</i> | 0 | 0 | 0.0012 1.2 |
| $ Y_1\rangle$ | 1.3×10^{-4} 4.9×10^{-4} | 0 | <i>14.4</i> <i>43.3</i> | 0.026 0.068 | | 0 | 0.0054 0.011 | 0.057 0.12 | 2.6 | 7.0×10^{-4} 0.91 |
| $ X_1\rangle$ | 3.9×10^{-5} 1.7×10^{-4} | 3.9 <i>14.4</i> | 0 | 4.9×10^{-4} 0.0015 | 0 | | 0.089 0.20 | 0.095 0.21 | 1.5 | 5.7×10^{-4} 0.83 |
| $ D_1\rangle$ | 0 | 2.1×10^{-5} 9.6×10^{-5} | 1.8×10^{-4} 6.6×10^{-4} | <i>0.14</i> <i>0.48</i> | 0.0024 0.0074 | 0.065 0.17 | | 0 | 0 | 3.9×10^{-4} 0.71 |
| $ Z_1\rangle$ | <i>0.013</i> <i>0.065</i> | 3.3×10^{-5} 1.5×10^{-4} | 1.3×10^{-4} 4.9×10^{-4} | 0 | 0.04 0.11 | 0.07 0.18 | 0 | | 0.062 | 3.8×10^{-4} 0.70 |

localized and unipolar nature of the isoelectronic potential could, indeed, result in capture times significantly different from that of quantum dots.

In conditions where the PL decay rate of photogenerated carriers in the surrounding bulk or quantum well is faster than the capture rate, nonresonant optical pumping becomes less efficient, and the PL yield is reduced. It also implies that the spin is lost through several bulk relaxation mechanisms before exciton capture. A better understanding of the capture mechanism and the identification of the limiting process appears necessary for a deeper analysis. Nonetheless, resonant excitation can be used to generate excitons and spin-polarized excitons through a relatively high dipole moment and convenient optical selection rules.

2. Spontaneous emission

The rate of spontaneous emission rate $\Gamma_0^{(\text{rad})}$ multiplied by the dipole moment of a given state results in the radiative rates listed in Table IV. The radiative recombination lifetimes associated with bright states range from 200 to 670 ps. These values are in good agreement with Rabi oscillations measurements that revealed radiative lifetimes on the order of 500 ps [11].

For z -polarized transitions, the rate is very high (5 ns⁻¹) for Z_2 and very low (0.06 ns⁻¹) for Z_1 . This is attributed to the fact that, as presented in Table I, a pure heavy-hole state has a vanishing dipole moment along the z axis. Therefore, Z_1 with its dominant heavy-hole composition is associated to a very low spontaneous emission rate.

3. Nonradiative emission

Figure 3(b) indicates that photoluminescence quenching is well represented by a single Arrhenius equation [$I(0)/I(T) - 1 = A \exp[-E_a/(k_B T)]$], where $I(0)$ is the extrapolated intensity at $T = 0$ and E_a is the activation energy] with $E_a = 5.1 \pm 0.1$ meV. However, this simple model is not strictly accurate as it supposes that all excitonic states share the same energy. The exciton dynamics model yields the temperature-dependent total intensity shown in Fig. 6(d). The activation energy ranges

from 4.7 meV for Z_2 (value shown in Table III) to 5.6 meV for Z_1 . The average value of 5.2 meV is similar to that obtained from the simple Arrhenius fit, which indicates that the exciton population tends to be uniformly distributed over all states as temperature increases.

The rather large value of $\Gamma_0^{(\text{nr})}$ leads to a significant variation of the nonradiative emission rate for different excitonic states (see Table IV). At 5 K, the nonradiative lifetime ranges from 0.4 μ s (Z_2) to 2.6 μ s (Z_1), while at 12 K it ranges from only 0.6 to 1.4 ns. Over 12 K, the rate of nonradiative emission overcomes the rate of spontaneous emission, and the photoluminescence signal completely disappears.

Taking into account the binding mechanism of excitons to isoelectronic impurities [50], quenching can be associated with (1) the escape of the hole leaving the electron bound to the nitrogen dyad, (2) the escape of the whole exciton (the free-exciton energy is 1.5141 meV), or (3) the escape of the electron and hole as uncorrelated particles (the free-electron and hole energy is 1.519 eV). For nitrogen dyads in GaP, it has been demonstrated [19,50] that the dominant mechanism depends on the binding energy of the nitrogen pair configuration: the first mechanism dominates for the deepest levels, and the second and third mechanisms dominate for shallower levels. For excitons bound to the nitrogen dyad emitting at 1.5078 meV in GaAs, PL experiments under hydrostatic pressure have suggested that hole escape can be clearly identified as the dominant mechanism only if the optical binding energy clearly exceeds the thermal activation energy [36]. In the case at hand, the binding energy of 6.3 meV is only slightly higher than the activation energy 5.2 meV, and our analysis cannot discriminate between both escape mechanisms.

4. Interlevel transfers

Acoustic-phonon-induced transfers. Longitudinal-acoustic phonons provide the impulse and energy to drive exciton transfers between exciton states of identical polarization. As seen from Table IV, these transfers considerably exceed those of exciton capture, radiative and nonradiative emission,

and hyperfine-mediated transfers at 12 K. Therefore, after being populated, an exciton state reaches thermodynamic equilibrium with its counterpart of similar polarization before other types of transfer occur. As a result, identical decay times for similarly polarized transitions are observed. At 5 K, phonon-induced transfer rates are comparable to radiative rates. Populations of similarly polarized states do not reach complete equilibrium, and a slight difference in photoluminescence decay times appears [see Fig. 6(a)].

Hyperfine interaction. Hyperfine interaction is a second-order process that allows transfer between dark or z -polarized states to x - and y -polarized states. Transfer rates are significantly lower than spontaneous emission rates of most optically active states and phonon-induced transfer rates. As can be seen from the data in Table IV, the dominant hyperfine transfers from X or Y states are to the closest Z or D states and vice versa. The relatively slow transfers from D to bright states explains the long PL decay time observed.

Depending on the initial state of the exciton, different processes leading to radiative decay predominates. Directly populated $X_{1,2}$ and $Y_{1,2}$ states most likely recombine radiatively (or nonradiatively if thermal energy is sufficient) before transferring to D or Z states. Similarly, Z_2 likely recombines radiatively before transfers to X or Y states occurs. In contrast, the weak dipole moment of Z_1 allows for exciton transfer prior to radiative recombination. According to Table IV, a fast acoustic phonon-mediated transfer to Z_2 occurs, where radiative recombination then takes place. Although these subnanosecond decay rates influence the PL dynamics, they are not directly observed as two slower processes mask their presence, as described next.

The PL decay time observed for Y transitions corresponds to the sum of several characteristic times associated with (1) the capture of an exciton in either dark state $D_{1,2}$, (2) the fast phonon-mediated transfer between D_1 and D_2 , (3) the dominant hyperfine transfer at 5 K to Y_2 , (4) phonon-mediated transfer, which efficiently mixes the population of Y_1 and Y_2 , and (5) radiative emission, which occurs from either one of these two states. Therefore, the PL decay time of Y states is dominated by the slowest processes, which in this case are the capture time and the hyperfine transfer. The PL decay time for X transitions can be explained in a similar fashion. In this case, however, phonon-mediated transfer from $D_{1,2}$ to $X_{1,2}$ is slower because of the larger energy splitting separating these states, which explains the longer decay time observed in Fig. 6.

In quantum dots, experimental relaxation times at low temperature ($T \leq 10$ K) are typically in the range of 10 to 20 ns. [51,52]. Assuming that hyperfine-induced relaxation dominates in this temperature regime, scaling down the number of interacting nuclei to match that of an IC bound electron should lead to much larger Overhauser field fluctuations [40] and significantly shorter relaxation times. However, this does not appear to be the case. For X_1 and Y_1 , hyperfine relaxation times are, respectively, 15 and 25 ns at 5 K. Because of D_2 and Z_2 positioned nearby, the relaxation times of X_2 and Y_2 are somewhat shorter, 5.0 and 1.8 ns. Although hyperfine interaction might possibly be enhanced by the smaller number of interacting nuclei, it appears that it does not significantly affect the exciton dynamics and that spin-relaxation times remain comparable to those observed from quantum dots.

Temperature evolution of the decay time. At low temperatures ($T < 2$ K), thermally activated processes are quenched, and dark excitons are trapped for a time scale significantly larger than the laser repetition rate. The PL decay time is therefore determined solely by the capture of bright excitons and their subsequent radiative recombination. As temperature increases, slow hyperfine transfers from long-lived D states to bright states are activated, leading to an increase in the observed PL decay times. The maximum decay time occurs at 3.2 K for Y transitions and at 4.7 K for X transitions. This difference is again explained by the larger energy separating X states from D states. In this intermediate range of temperatures (2–5 K), interlevel transfers mediated by LA phonons are too slow to bring the exciton populations to thermodynamic equilibrium, and dissimilar decay times are observed for transitions with similar polarizations. At higher temperatures, decay times are dominated by the capture of dark excitons and their hyperfine transfer to bright states. Over 10 K, decay times decrease faster because nonradiative recombination starts to overcome every other mechanism.

Temperature evolution of relative PL intensities. Intensities are proportional to integrated occupation probabilities and radiative decay rates. In the limit of relatively high temperature ($T \geq 12$ K), thermal energy is sufficient to equalize occupation probabilities of all states. Relative intensities are then proportional to radiative decay rates. As temperature is reduced, occupation probabilities are higher for lower-energy states, and the relative intensity of X_1 and Y_1 increases at the expense of X_2 and Y_2 .

VI. CONCLUSION

We have presented an extensive study of the recombination dynamics of excitons bound to nitrogen dyads in GaAs, which present a rich and complex behavior depending sensitively on temperature, on symmetry representation, and on the light- and heavy-hole content of the exciton states involved. Through a simulation of the experimental data using a comprehensive model, we were able to identify the nature of the mechanisms governing the recombination dynamics and to extract quantitative information on these processes. We have identified that exciton capture and interlevel transfers mediated by the hyperfine interaction are slow processes responsible for the slow and anisotropic decay times experimentally observed. Furthermore, we have demonstrated that deformations induced by LA phonons couple heavy and light holes. This phenomenon is relatively unique to systems with nearly degenerate light- and heavy-hole states and leads to efficient transfers between states of similar symmetry representation. We also extracted numerical values for the radiative and nonradiative emission rates, which agree with previously reported values.

These findings significantly enhance our understanding of the dynamics of excitons bound to ICs and suggest that they are interesting candidates for the realization of electron qubits. Indeed, the electron spin flip mediated by the hyperfine interaction is not significantly enhanced and remains comparable to that of quantum dots. Interestingly, much longer relaxation times should be obtained from ICs in a host with fewer nuclear spins, such as Si or II–VI semiconductors.

- [1] J. Berezovsky, M. H. Mikkelsen, N. G. Stoltz, L. A. Coldren, and D. D. Awschalom, *Science* **320**, 349 (2008).
- [2] D. Press, T. D. Ladd, B. Zhang, and Y. Yamamoto, *Nature (London)* **456**, 218 (2008).
- [3] M. V. G. Dutt, L. Childress, L. Jiang, E. Togan, J. Maze, F. Jelezko, A. S. Zibrov, P. R. Hemmer, and M. D. Lukin, *Science* **316**, 1312 (2007).
- [4] G. D. Fuchs, G. Burkard, P. V. Klimov, and D. D. Awschalom, *Nat. Phys.* **7**, 789 (2011).
- [5] J. J. Pla, K. Y. Tan, J. P. Dehollain, W. H. Lim, J. J. L. Morton, D. N. Jamieson, A. S. Dzurak, and A. Morello, *Nature (London)* **489**, 541 (2012).
- [6] A. M. Tyryshkin, S. Tojo, J. J. L. Morton, H. Riemann, N. V. Abrosimov, P. Becker, H.-J. Pohl, T. Schenkel, M. L. W. Thewalt, K. M. Itoh *et al.*, *Nat. Mater.* **11**, 143 (2012).
- [7] F. Jelezko and J. Wrachtrup, *Phys. Status Solidi A* **203**, 3207 (2006).
- [8] Y. G. Zhang, Z. Tang, X. G. Zhao, G. D. Cheng, Y. Tu, W. T. Cong, W. Peng, Z. Q. Zhu, and J. H. Chu, *Appl. Phys. Lett.* **105**, 052107 (2014).
- [9] G. Pica, G. Wolfowicz, M. Urdampilleta, M. L. W. Thewalt, H. Riemann, N. V. Abrosimov, P. Becker, H.-J. Pohl, J. J. L. Morton, R. N. Bhatt *et al.*, *Phys. Rev. B* **90**, 195204 (2014).
- [10] I. Aharonovich and M. Toth, *Nat. Phys.* **10**, 93 (2014).
- [11] G. Éthier Majcher, P. St-Jean, G. Boso, A. Tosi, J. F. Klem, and S. Francoeur, *Nat. Commun.* **5**, 3980 (2014).
- [12] S. Francoeur, J. F. Klem, and A. Mascarenhas, *Phys. Rev. Lett.* **93**, 067403 (2004).
- [13] M. Ikezawa, Y. Sakuma, and Y. Masumoto, *Jpn. J. Appl. Phys.* **46**, L871 (2007).
- [14] M. Jo, T. Mano, T. Kuroda, Y. Sakuma, and K. Sakoda, *Appl. Phys. Lett.* **102**, 062107 (2013).
- [15] A. Muller, P. Bianucci, C. Piermarocchi, M. Fornari, I. C. Robin, R. André, and C. K. Shih, *Phys. Rev. B* **73**, 081306 (2006).
- [16] S. Marcet, C. Ouellet-Plamondon, G. Éthier-Majcher, P. Saint-Jean, R. André, J. F. Klem, and S. Francoeur, *Phys. Rev. B* **82**, 235311 (2010).
- [17] F. Sarti, G. Munoz Matutano, D. Bauer, N. Dotti, S. Bietti, G. Isella, A. Vinattieri, S. Sanguinetti, and M. Gurioli, *J. Appl. Phys.* **114**, 224314 (2013).
- [18] M. Ikezawa, Y. Sakuma, L. Zhang, Y. Sone, T. Mori, T. Hamano, M. Watanabe, K. Sakoda, and Y. Masumoto, *Appl. Phys. Lett.* **100**, 042106 (2012).
- [19] P. St-Jean, G. Éthier-Majcher, Y. Sakuma, and S. Francoeur, *Phys. Rev. B* **89**, 075308 (2014).
- [20] O. Labeau, P. Tamarat, and B. Lounis, *Phys. Rev. Lett.* **90**, 257404 (2003).
- [21] P. R. C. Kent and A. Zunger, *Phys. Rev. B* **64**, 115208 (2001).
- [22] S. Francoeur and S. Marcet, *J. Appl. Phys.* **108**, 043710 (2010).
- [23] C. Ouellet-Plamondon, S. Marcet, J. Klem, and S. Francoeur, *J. Lumin.* **131**, 2339 (2011).
- [24] S. Marcet, C. Ouellet-Plamondon, J. F. Klem, and S. Francoeur, *Phys. Rev. B* **80**, 245404 (2009).
- [25] G. Fishman and G. Lampel, *Phys. Rev. B* **16**, 820 (1977).
- [26] D. J. Hilton and C. L. Tang, *Phys. Rev. Lett.* **89**, 146601 (2002).
- [27] R. I. Dzhiyev, V. L. Korenev, I. A. Merkulov, B. P. Zakharchenya, D. Gammon, A. L. Efros, and D. S. Katzer, *Phys. Rev. Lett.* **88**, 256801 (2002).
- [28] P.-F. Braun, X. Marie, L. Lombez, B. Urbaszek, T. Amand, P. Renucci, V. Kalevich, K. Kavokin, O. Krebs, P. Voisin *et al.*, *Phys. Rev. Lett.* **94**, 116601 (2005).
- [29] B. Eble, C. Testelin, P. Desfonds, F. Bernardot, A. Balocchi, T. Amand, A. Miard, A. Lemaître, X. Marie, and M. Chamarro, *Phys. Rev. Lett.* **102**, 146601 (2009).
- [30] T. Flissikowski, I. A. Akimov, A. Hundt, and F. Henneberger, *Phys. Rev. B* **68**, 161309 (2003).
- [31] S. Laurent, B. Eble, O. Krebs, A. Lemaître, B. Urbaszek, X. Marie, T. Amand, and P. Voisin, *Phys. Rev. Lett.* **94**, 147401 (2005).
- [32] D. Heiss, S. Schaeck, H. Huebl, M. Bichler, G. Abstreiter, J. J. Finley, D. V. Bulaev, and D. Loss, *Phys. Rev. B* **76**, 241306 (2007).
- [33] A. V. Khaetskii and Y. V. Nazarov, *Phys. Rev. B* **61**, 12639 (2000).
- [34] E. Tsitsishvili, R. v. Baltz, and H. Kalt, *Phys. Rev. B* **72**, 155333 (2005).
- [35] D. V. Bulaev and D. Loss, *Phys. Rev. Lett.* **95**, 076805 (2005).
- [36] X. Liu, M.-E. Pistol, and L. Samuelson, *Phys. Rev. B* **42**, 7504 (1990).
- [37] M.-F. Tsai, H. Lin, C.-H. Lin, S.-D. Lin, S.-Y. Wang, M.-C. Lo, S.-J. Cheng, M.-C. Lee, and W.-H. Chang, *Phys. Rev. Lett.* **101**, 267402 (2008).
- [38] I. A. Merkulov, A. L. Efros, and M. Rosen, *Phys. Rev. B* **65**, 205309 (2002).
- [39] D. Gammon, A. L. Efros, T. A. Kennedy, M. Rosen, D. S. Katzer, D. Park, S. W. Brown, V. L. Korenev, and I. A. Merkulov, *Phys. Rev. Lett.* **86**, 5176 (2001).
- [40] S. I. Erlingsson, Y. V. Nazarov, and V. I. Fal'ko, *Phys. Rev. B* **64**, 195306 (2001).
- [41] J. Puebla, E. A. Chekhovich, M. Hopkinson, P. Senellart, A. Lemaître, M. S. Skolnick, and A. I. Tartakovskii, *Phys. Rev. B* **88**, 045306 (2013).
- [42] P. Fallahi, S. T. Yilmaz, and A. Imamoglu, *Phys. Rev. Lett.* **105**, 257402 (2010).
- [43] E. A. Chekhovich, A. B. Krysa, M. S. Skolnick, and A. I. Tartakovskii, *Phys. Rev. Lett.* **106**, 027402 (2011).
- [44] E. Tsitsishvili and H. Kalt, *Phys. Rev. B* **82**, 195315 (2010).
- [45] B. Krummheuer, V. M. Axt, and T. Kuhn, *Phys. Rev. B* **65**, 195313 (2002).
- [46] L. Besombes, K. Kheng, L. Marsal, and H. Mariette, *Phys. Rev. B* **63**, 155307 (2001).
- [47] U. Bockelmann, *Phys. Rev. B* **48**, 17637 (1993).
- [48] T. Takagahara, *Phys. Rev. B* **60**, 2638 (1999).
- [49] C. Tonin, R. Hostein, V. Voliotis, R. Grousson, A. Lemaître, and A. Martinez, *Phys. Rev. B* **85**, 155303 (2012).
- [50] M. Sturge, E. Cohen, and K. Rodgers, *Phys. Rev. B* **15**, 3169 (1977).
- [51] H. Kurtze, D. R. Yakovlev, D. Reuter, A. D. Wieck, and M. Bayer, *Phys. Rev. B* **85**, 195303 (2012).
- [52] I. Favero, G. Cassabois, C. Voisin, C. Delalande, P. Roussignol, R. Ferreira, C. Couteau, J. P. Poizat, and J. M. Gérard, *Phys. Rev. B* **71**, 233304 (2005).